Calibration of the Solar Orbiter antennas by Rheometry and computer simulations (Scientific part)

Scientific Report on FFG/ASAP 11 project SOLOCAL

by
Dr. Mykhaylo Panchenko
DI Dr. Georg Fischer
Dr. Wolfgang Macher

Apr 2017 / Final report

Contents

Executive Summary

We report results of the analysis of electric antennas properties of RPW (Radio and Plasma Wave) instrument on board Solar Orbiter mission the launch of which is planned in October 2018. The studies were performed in the frame of the Austrian Research Promotion Agency (FFG) project SOLOCAL at the Space Research Institute of the Austrian Academy of Sciences in Graz from 1 June 2015 to 31 July 2016. Solar Orbiter/RPW will measure magnetic and electric fields at using a number of sensors/antennas, and it will determine the characteristics of electromagnetic and electrostatic waves in the solar wind from almost DC to 16 MHz using a set of electric antennas and a search coil magnetometer. RPW antenna system consists of a set of three identical monopoles (6.5 m length) deployed from two corners and one side of the spacecraft. These three monopoles (PZ, PY and MY) are 125°, 110° and 125° apart, in a plane perpendicular to the spacecraft-Sun axis.

The complex interaction between spaceborne antennas and metallic structures or other spacecraft electric instruments causes distortion of the antenna reception properties. As result the effective directivity of the antennas differ from the expected. The main goal of this contracted SOLOCAL project was to provide a set of calibration data of the RPW antennas which will be used for accurate evaluation of scientific data. The true antenna properties have been determined using two independent methods - numerical computer simulations and experimental rheometry technique.

The first part of this project was to perform numerical computer simulations with a detailed spacecraft model derived from an original CAD model of Solar Orbiter and RPW antennas. This original CAD model has been simplified removing many fine structures and inner parts which were not necessary for our simulations. In the course of the project several CAD models with different levels of details, different position of the solar panels and various thermal bends of the antennas have been designed. Then these models were imported into a CADFEKO tool, which is used to construct a mesh model for FEKO code. The numerical simulations were based on a program package FEKO, which is a highly sophisticated commercial antenna simulation tool. The current distribution of the antenna-spacecraft system calculated by FEKO has been used to retrieve the RPW antenna reception properties by means of MATLAB SAT toolbox library - our in-house toolbox which was developed by IWF in the recent years.

We have retrieved effective length vectors of the antennas (length and axes) in quasi-static frequency regime for open feeds. The effective vector of the antenna represents the electrically effective direction and length of each antenna, in contrast to the physical (mechanical) antenna rod. The results show that effective lengths vectors of Pz, Py and My antennas are offset from the mechanical axes by about 9° (for Pz), 14°(Py) and 14°(My) towards the positive X-axis while the physical antennas are coplanar in the YZ-plane. It was found that the azimuthal angles of the effective axes are not altered by the presence of the spacecraft structure. The effective lengths of the Pz, Py and My antenna are about 4.4 m, 3.9 m and 3.9 m correspondingly. These lengths are smaller than length of the antenna rods (6.5 m). In order to find the effective length vectors for the

loaded antenna, we also determined the antenna capacitance matrix. The calculated antenna impedances are about 71 - 72 pF for each of the antenna which is in good agreement with theoretical estimations (69 pF). The impedances are dominantly capacitive. The directivity patterns and impedances of the antenna have were also simulated up to frequencies of 16 MHz. Far-field directivity patterns have smooth toroidal shape up to the resonance frequency at ~10.5 MHz where the radiation antenna pattern develops complex lobes.

Moreover we simulated antenna reception properties for different position of the rotatable solar panels which can be turned up to 45 degrees out of the vertical position during different phases of the mission. Our simulations showed no significant influences of the solar panel rotation on the resulting effective antenna vectors.

The other task in frame of the performed numerical simulations was to study the influence of a thermal bend of the antennas on the reception properties. It is expected that there will be a large temperature gradient as result of an uneven illumination, which, in turn will result in a mechanical deformations which bends the antennas away from the Sun. The thermal bend estimated by CNES engineers can be more than 1.2 m at the distance of 0.22 AU. We simulated the reception antenna properties for different thermal bends form 0 to 1.4 m. The results clearly show that due to the thermal deformation the offset of the effective length vectors is reduced to 4°, 10° and 10° (for Pz, Py and My antennas) for the thermal bend of 1.4 m. We provided the effective antenna vectors for different thermal deformations which will correspond to different orbital phases of the Solar Orbiter mission.

We have also performed additional simulations concerning the accuracy of inflight-calibration of the RPW antennas based on observations of Terrestrial Auroral kilometric radiation (AKR). These measurements are planned at the initial phase of the Solar Orbiter mission. The simulations show that the effective length vectors of RPW antennas can be determined very accurate for the scheduled roll maneuvers on 12 – 26 Oct., 2018 and 12 – 17 Dec., 2021. In the same time, the interval of roll maneuvers on 15 – 20 Feb., 2020 is unfavorable for the in-flight calibration.

The second part of the project was to perform the experimental measurements of the antenna reception properties by means of Rheometry technique which uses a down-scaled gold-plated model of the spacecraft. The method is based on electrolytic tank measurements which allow us to determine the effective axes and lengths of the antennas for the quasi-static frequency range. The hardware model is immersed in the tank filled with tap water. A signal generator is connected to the plates, attached to two opposite sides of the tank, to sustain a homogeneous electric field. The voltages at the model antennas are measured as a function of the model orientation. The Rheometry measurements were performed using 1:50 scaled model of Solar Orbiter which was developed in the frame of the ESA funded project “Anechoic chamber measurements”. The model has updated to include new 6.5 m (in scale 1:50) length antennas. The resulting quantities are similar to the results obtained from the numerical simulation.

1. Introduction

The complex interaction between spaceborne antennas and metallic structures or other spacecraft electric instruments causes distortion of the antenna reception properties. As result the effective directivity of the antennas differ from the expected. Owing to the complex structure of the antenna spacecraft system, it is impossible to find either analytical closed form solutions, or experimental solutions, for such antennas onboard the spacecraft, hence the need to perform scale model measurements or computer simulations. The main goal of this study was to perform Rheometry measurements and computer simulations of RPW antennas onboard Solar Orbiter.

1.1 The Solar Orbiter mission

Solar Orbiter is an ESA M class mission that is planned to be launched in October 2018. The spacecraft will enter an elliptical orbit around Sun with a perihelion as low as 0.28 AU. Its inclination will be increased up to 25 degree's with respect to the solar equator. The close distance to the Sun and the partial co-rotation of Solar Orbiter with the Sun should allow observations of solar features and their connection to the heliosphere for much longer periods than from near-Earth vantage points. Details can be found on ESA's website (http://sci.esa.int/solar-orbiter).

Solar Orbiter's mission is to address the central question of heliophysics: How does the Sun create and control the heliosphere? This, in turn, is a fundamental part of the second science question of ESA's Cosmic Vision: "How does the solar system work?" Solar Orbiter is specifically designed to identify the origins and causes of the solar wind, the heliospheric magnetic field, solar energetic particles, transient interplanetary disturbances, and even the Sun's magnetic field itself.

The science payload of Solar Orbiter comprises remote-sensing instruments (imaging in the visible, UV, EUV and X-ray) which will preferentially observe the Sun from close distance and high latitudes. In-situ instruments should operate continuously to measure the magnetic field, the plasma waves, and the particle properties in the solar wind.

1.2 Radio and Plasma Waves (RPW) radio instrument on-board Solar Orbiter.

The Radio and Plasma Waves (RPW) experiment is unique amongst the Solar Orbiter instruments in that it makes both in-situ and remote-sensing measurements. RPW will measure magnetic and electric fields at high-time resolution using a number of sensors/antennas, and it will determine the characteristics of electromagnetic and electrostatic waves in the solar wind from almost DC to 16 MHz. The Principal Investigator of the RPW instrument is Dr. Milan Maksimovic from the Observatoire de Paris, LESIA, France. RPW consists of:

- The Low Frequency Receiver (LFR). LFR covers both in-situ electric and magnetic measurements from DC to about 10 kHz and will provide both waveform and power spectra in this frequency range. High-level processed data (polarization and propagation properties

of the observed waves), with various data rate possibilities (continuous or cyclic transmission, adaptable frequency bandwidth, as well as adaptable frequency and time resolutions) will also be provided by LFR.

- The Thermal Noise and High Frequency receiver (TNR‑HFR). TNR‑HFR will determine properties of the ambient electron population from measurements of the local thermal noise around the plasma frequency and remotely detect solar radio emissions. It will provide, at various temporal resolutions, electric power spectra from 4 kHz up to 16 MHz and magnetic power spectral densities from 4 kHz up to 500 kHz.
- The Time Domain Sampler (TDS). TDS will perform digitization of the electric and magnetic field waveforms in the frequency range from 100 Hz to 250 kHz. These will be pre-processed and a selection of potentially interesting events will be stored in internal memory and later transmitted to the ground.

These three sub-systems (LFR, TNR‑HFR, TDS) are connected to two different sensor units: a set of electric antennas (ANT) and a search coil magnetometer (SCM). The ANT sensor design is optimized to measure both DC/low frequency electric fields and higher frequency radio and thermal noise emissions.

1.3 Methods of RPW antenna calibration

The highly conducting spacecraft body is electromagnetically coupled to the antennas and, therefore, the antenna receiving properties strongly depend on the spacecraft shape. It is impossible to find an analytical solution of the surface current distribution in closed form, owing to the complex structure of the antennas-spacecraft system. Therefore the computer simulation and experimental methods are used to find the reception properties of the antennas. The reception properties of Solar Ortbiter/RPW antennas have been investigated by means of two methods: 1) Numerical computer simulations and 2) Rheometry measurements.

1) **Numerical simulations with electromagnetic code FEKO.** A very powerful technique to analyze the reception properties of the spaceborne antennas is a computer-based wire or patch-grid simulation in which the spacecraft body and antennas are modeled as mesh of wires or patches [Fischer et al., 2001; Oswald et al., 2009; Sampl et al., 2011, Rucker et al., 2011]. Numerical solutions of the electric and magnetic field integral equations by means of numerical electromagnetic codes yield the satisfying determination of the antenna effective length vectors and antenna radiation pattern for quasi-static as well as for higher frequency range. We applied the program package **FEKO**, which is a highly sophisticated commercial antenna simulation tool based on the solution of the electric field integral equation. The current distribution on the antenna-spacecraft system calculated by FEKO are used to retrieve the antenna properties such as radiation patterns, effective antenna vectors (axes and

lengths), and antenna impedances. In these calculations we utilized MATLAB SAT toolbox library developed at the Space Research Institute of the Austrian Academy of Sciences [Macher and Vejda, 2003; Sampl, 2011]

2) **Rheometry**. This method is based on electrolytic tank measurements where the scaled (in our case 1:50) gold plated model is immersed in a water-filled tank. Metal plates are connected to a signal generator forming a large capacitor with homogeneous electric field in the tank. A voltmeter is connected to the antenna terminal and the induced voltages are measured depending antenna orientation with regard to direction of the electric field in the tank. The Solar Orbiter model could rotate around two different suspension axes. This technique allows us to determine the effective length vectors of the antennas as well as the antenna capacitance matrix in the quasi-static frequency range. The rheometry method have been applied for the precise calibration of the space-borne antennas onboard Cassini-RPWS (Rucker et al., 1996), Interball/POLRAD (Panchenko, 2004), STEREO/WAVES (Oswald et al., 2006, 2009; Rucker et al., 2005), Resonance (Sampl et al, 2009) and Juno missions.

2. Solar Orbiter RPW antenna design and CAD modelling

The Solar orbiter RPW antenna system consists of a set of three identical monopoles (6.5 m length) deployed from two corners and one side of the spacecraft. These three monopoles (PZ, PY and MY) are 125°, 110° and 125° apart, in a plane perpendicular to the spacecraft-Sun axis (Fig. 1). Each monopole consists of a rigid deployable boom (0.98 m) with thermal shields and an antenna conical stroke with 6.5 m length (Figure 2).

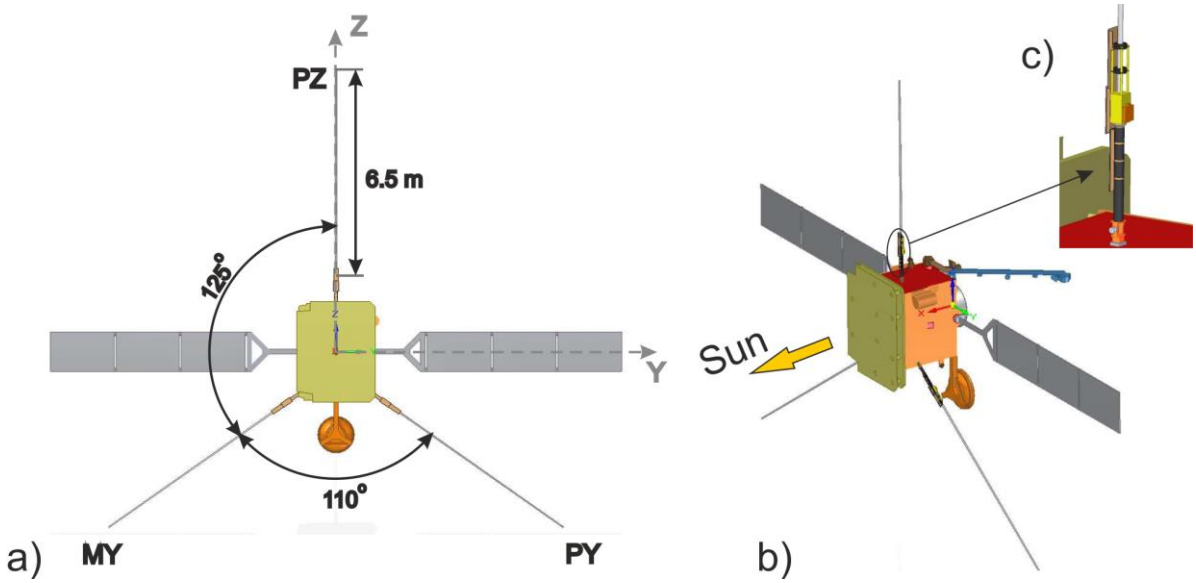

Figure 1. RPW electric sensors consist of three antennas (PZ, PY and MY) mounted on booms (panel a). Panel b) shows the 3D view of Solar Orbiter based on the reduced CAD model. Panel c) shows the details of antenna boom with thermal shields.

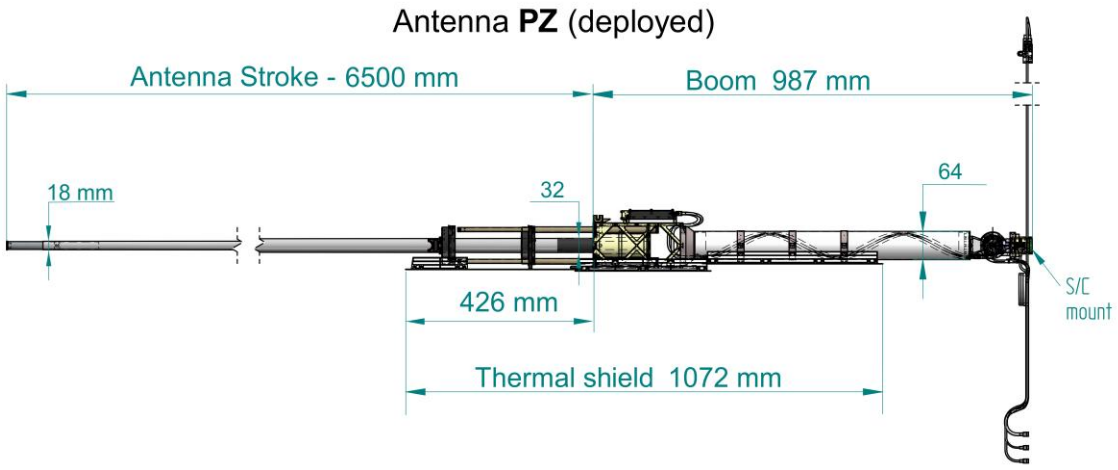

Figure 2. Design of deployed PZ antenna of the PRW. Dimensions are in millimeters. The antenna system consists of deploying mechanism, ~1 m boom, and 6.5 m length antenna stroke. Additionally, there are thermal shields in form of niobium plates.

2.1. Spacecraft surface-mesh modelling

The highly conducting spacecraft body is electromagnetically coupled to the antennas and, therefore, the antenna receiving properties strongly depend on the spacecraft shape. The numerical simulations of the Solar Orbiter/RPW antennas are based on a patch grid model covering the spacecraft features. We have obtained from RPW team the detailed CAD model with "stacer" type antennas and deployment booms. The original CAD model of the antennas consists of a great amount of details which are not necessary for our simulations. In general, increasing level of detail in the model returns diminishing gains in accuracy. Therefore we have built reduced model of the antennas where many fine structures and inner parts have been either removed or simplified. The spacecraft structures which are most important with regard to the antenna properties are central spacecraft body with heat shields, solar panels, HG antenna, instrumental and antenna booms and the RPW antennas. Since the size of the booms of the RPW antennas are comparable to the solar panels which are in close proximity, more detailed modelling was necessary in this area. The reduced model represents a compromise between structure detail and minimal number of surfaces which were needed to correct modelling of the antenna system.

Models were prepared with CAD program Solid Edge. Several CAD models with different levels of details, different position of the solar panels and various thermal bends of the antennas have been designed. The example of the simplified CAD model is shown in Fig. 1. The models were imported into a CADFEKO tool, which is used to construct a mesh model for FEKO code. The final model consists of about 9000 triangles and about 1950 curvilinear segments (Fig. 3). The current distribution of the antenna-spacecraft system calculated by FEKO has been used to retrieve the RPW antenna reception properties by means of MATLAB SAT toolbox library - our in-house toolbox which was developed by IWF in the recent years.

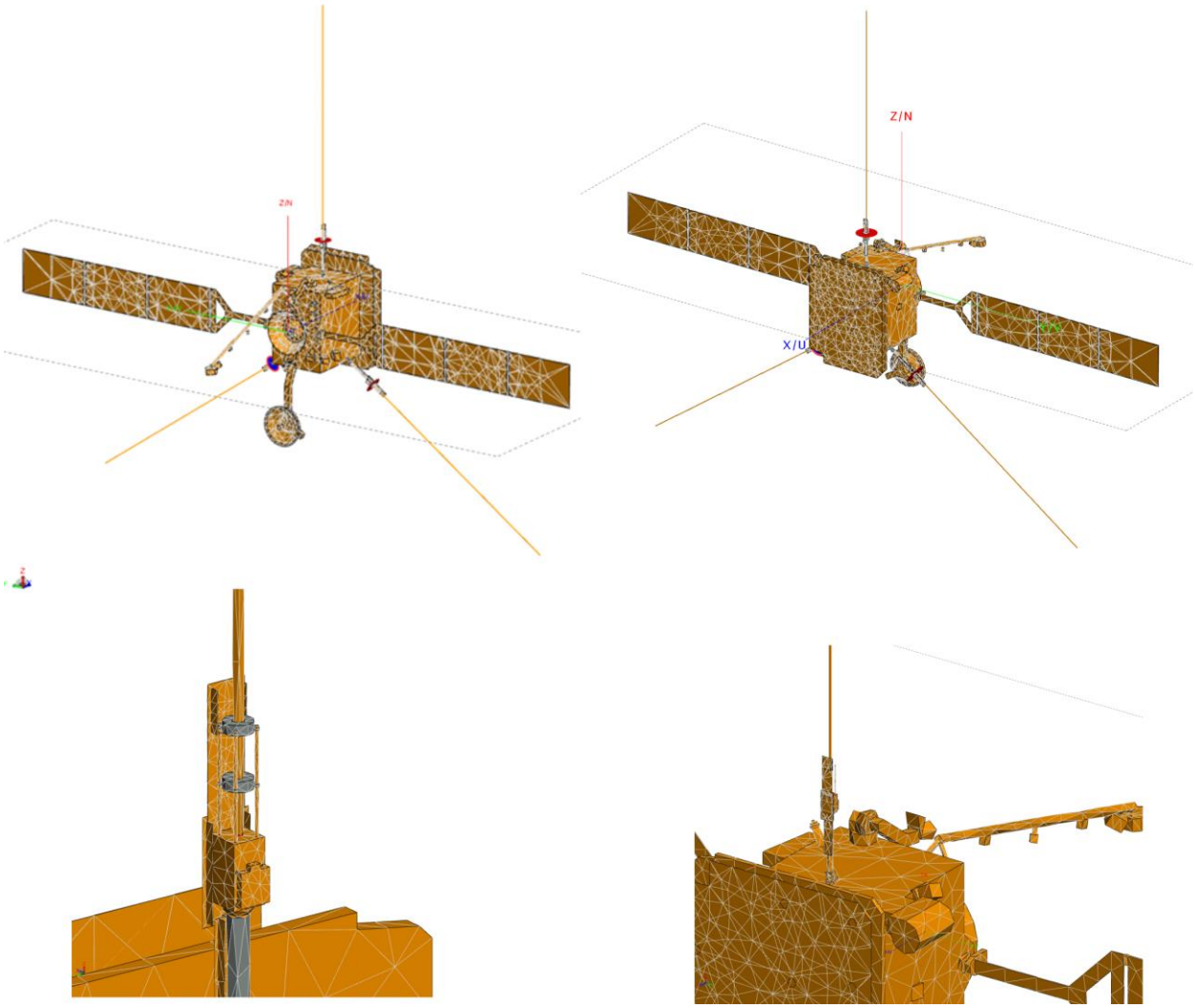

Figure 3. Mesh model of the Solar Orbiter generated by FEKOCAD out of the simplified CAD model. The model consists of 9014 triangles and 1947 curvilinear segments.

2.2 Reference coordinate system.

We used the same spherical coordinate system for CAD model, FEKO numerical simulations, physical scale models and rheometry measurements (Figure 4). The position of each antenna is described in spherical coordinates by colatitude angle θ and azimuth angle φ and the lengths of the antennas are denoted as **h.** The colatitude θ is defined with respect to the Z spacecraft axis and azimuth φ is defined in the XY spacecraft plane starting at the X-axis. The orientation of the Solar Orbiter/RPW antennas with their lengths is provided in Table 1. For the description of the effective antenna vectors we also used an angular separation angle γ which describes the angular offset of the effective antenna vector with respect to the physical position of the antenna (Fig. 4).

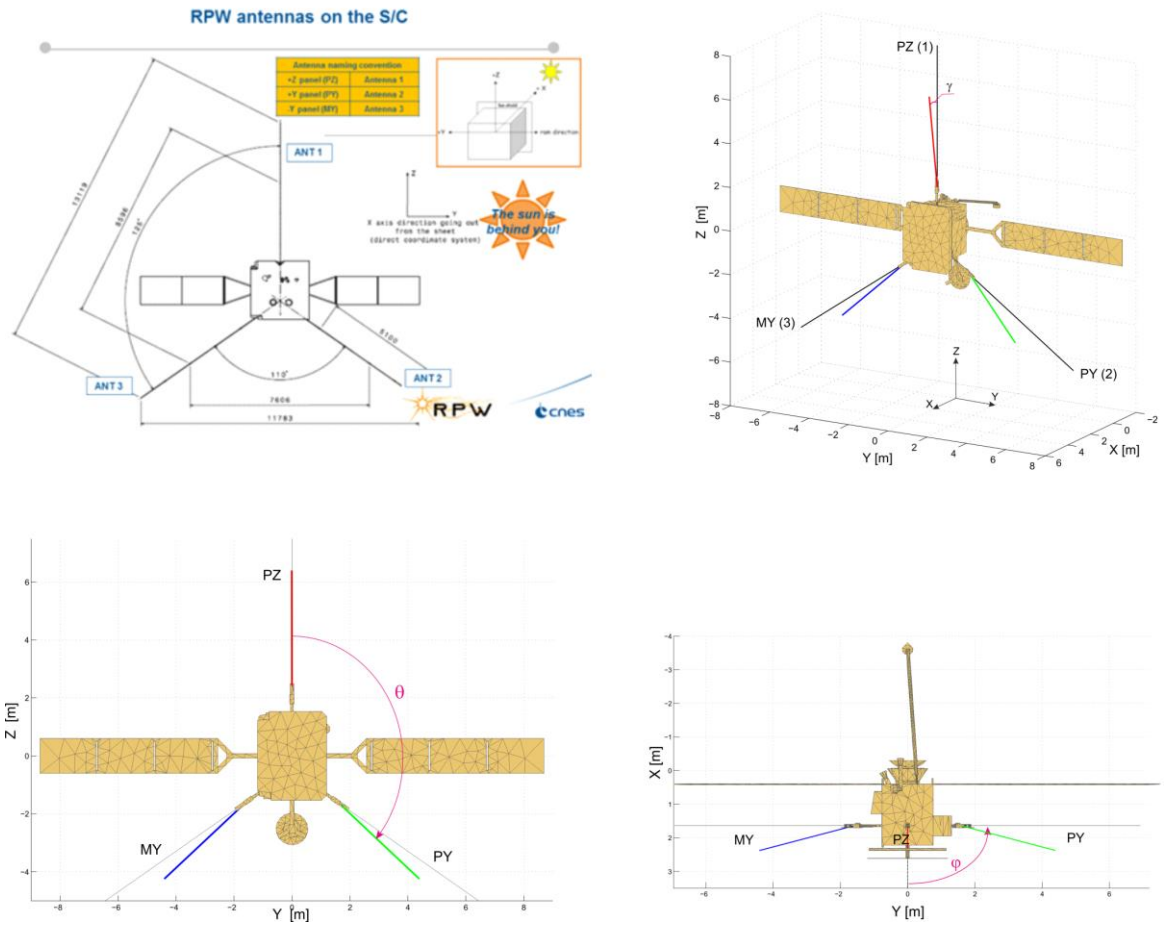

Figure 4. Reference frame coordinate system for the Solar Orbiter spacecraft. Panel a) shows the orientation of the spacecraft axes X, Y and Z with respect to the Sun and position of the RPW antennas. Panels c) and d) show the definition of the spherical coordinates: colatitude angle θ and azimuth angle φ. θ is defined with respect to the Z spacecraft axis and φ is azimuth angle in XY spacecraft plane starting at the X-axis. The effective antenna vectors are shown as the color lines. Angle γ describes the angular offset of the effective antenna axis with respect to the antenna physical position (panel b).

Table 1. Orientation of the Solar Orbiter/RPW antennas: θ – colatitude , φ – azimuth and h – lengths.

ANT	Mechanical antennas		
	h, m	θ, deg	φ, deg
PZ	6.5	0.0	0.0
PY	6.5	125	90
MY	6.5	125	-90

3. Antenna calculations using FEKO

FEKO (http://www.altairhyperworks.com/product/FEKO) is a highly sophisticated commercial antenna simulation tool based on the solution of the electric field integral equation. This program package includes not only time-frequency electromagnetic domain solvers but also 3D Parasolid CAD modelling interface (CADFEKO) and comprehensive post-processing and visualization tool POSTFEKO.

3.1 Effective length vectors

The open-circuit voltages on each short electrical dipole (or input voltages at each receiver channel) can be expressed as:

$$V_i = \boldsymbol{h}_i \cdot \boldsymbol{E} \qquad (1)$$

where $\boldsymbol{h}_i$ is an effective antenna length vector, $\boldsymbol{E}$ is the electric wave vector of the incoming wave and i denotes the antenna. Each $\boldsymbol{h}_i$ vector is represented by the following spherical coordinates: the antenna length h_e and the colatitude θ and the azimuth φ angles. The effective vector of the antenna represents the electrically effective direction and length of each antenna, in contrast to the physical (mechanical) antenna. The open port effective length vector of each antenna is given by the equation:

$$\boldsymbol{h}_i^o = \frac{1}{I_i} \int \boldsymbol{I}(\boldsymbol{r}) ds \qquad (2)$$

where I_i is the current at the feed of the i-th antenna, $\boldsymbol{I}(\boldsymbol{r})$ is the induced current distribution and *ds* is the infinitesimal line element along the respective wire segment. The integral runs over all segments of the wire grid. We used the program package FEKO for the calculation of the current distribution for each antenna. A typical current distribution is shown Figure 5. Areas around the excitation zone have a high current density.

The effective length vectors (Eq. 2) were calculated by means of a MATLAB SAT toolbox library [Fischer, 2000; Macher and Rucker, 1999; Macher and Vejda, 2003]. This toolbox uses the current distribution on the antenna-spacecraft system calculated by the FEKO to determine also other antenna properties such as radiation patterns and antenna impedances.

3.2 Quasi-static results

Although the effective antenna vector (Eq. 1) is a complex quantity, in quasi-static frequency range, when the radio wavelength is much greater than the size of the antenna system $L_{ant} \ll \lambda_{wave}$, $\boldsymbol{h}_i$ is real (imaginary part is negligible) and constant (independent of direction). The effective antenna length vectors on higher frequencies will be significantly different, especially for frequencies close to the antenna resonances [e.g. Oswald et al., 2009] (see section 3.5).

The first simulations have been performed for quasi-static frequency range i.e. at 300 kHz. We have retrieved the effective length vectors of the antennas (length and directions) for open feeds

including open port capacitance matrix and antenna impedances.

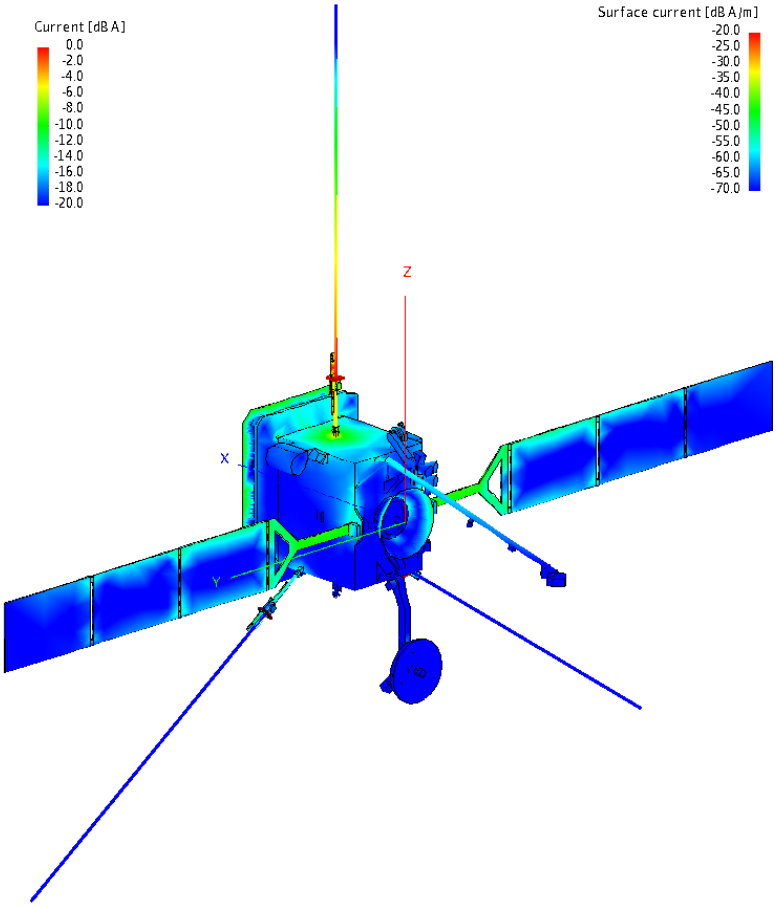

Figure 5. Surface currents [dB A/m] and line currents [dB A] for the Solar Orbiter model with antenna PZ driven with 1V at 300 kHz. The currents are normalized values. Feed zone of the PZ antenna have a high current density.

3.2.1 Open ports

The open port effective length vectors represent the reception properties of the bare antenna system without taking into account a total base capacitance composed of receiver input impedances and capacities of cable and antenna mounting structures. The determined effective length vectors of RPW monopoles for open feeds at 300 kHz are shown in Table 2 and Figure 6. The RPW instrument can also be operated in a dipole mode when the pairs of the antennas forms pseudo dipoles PZ-PY, PY-MY and MY-PZ. The effective vectors of these dipoles have been calculated by subtracting the corresponding effective vectors of the monopoles, e.g. $\mathbf{h}_e^{PZ\text{-}PY} = \mathbf{h}_e^{PZ} - \mathbf{h}_e^{PY}$, where $\mathbf{h}_e^{PZ\text{-}PY}$ is the effective vector of PZ-PY dipole, and $\mathbf{h}_e^{PZ}$ and $\mathbf{h}_e^{PY}$ are effective vectors of PZ and PY monopoles. The results are given in Table 2 and illustrated in Figure 7.

Table 2. Effective length vectors of PZ, PY and MY monopoles and PZ-PY, PY-MY and MY-PZ dipoles compared with physical position of the RPW antennas for open ports. h is antenna length, θ is colatitude and φ is azimuth angle. The angle γ is the angular separation between effective antenna vector and real antenna rod (see Fig. 4). The pseudo dipoles in the Table mean the vectors calculated as differences between corresponding monopoles forming the dipoles. The effective vectors of the dipoles have been calculated from the effective vectors of the corresponding monopoles.

ANT	Mechanical antennas			Effective antenna vectors			
	h, m	θ, deg	φ, deg	h_e, m	θ, deg	φ, deg	γ, deg
PZ	6.5	0.0	0.0	4.41	9.1	-0.4	9.1
PY	6.5	125	90	3.91	132.2	75.2	13.6
MY	6.5	125	-90	3.91	132.3	-75.2	13.6
	Pseudo-dipoles			Effective vectors of dipoles			
Dip. PZ-PY	11.53	152.5	90	7.53	158.1	-90.9	5.6
Dip. PY-MY	10.65	90.0	90	5.60	90.00	90.0	0.0
Dip. MY-PZ	11.53	152.5	-90	7.53	158.2	-89.1	5.6

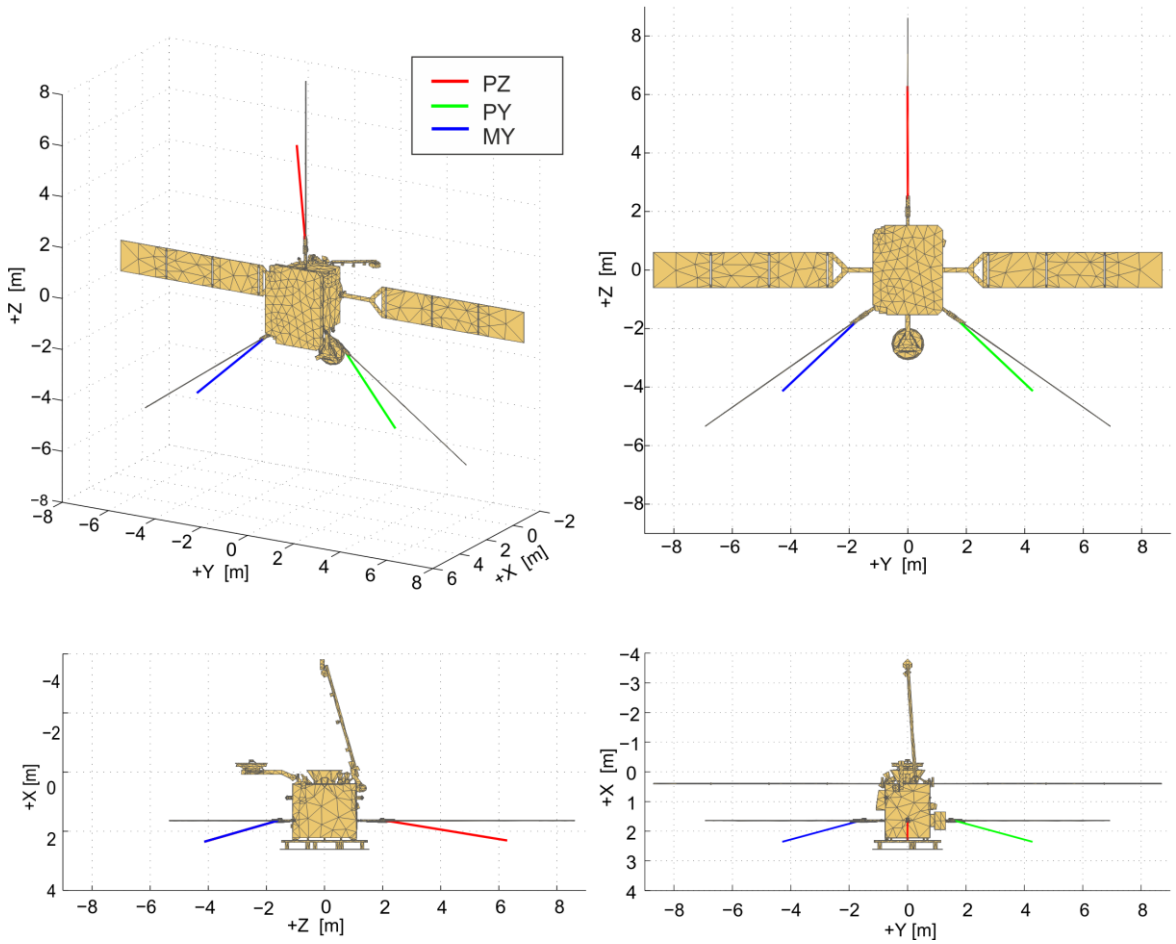

Figure 6. Effective length vectors at 300 kHz for a monopole configuration. Real antennas are given in black while the effective vectors are drawn in color. This gives an impression of the difference between mechanical and electrical quantities.

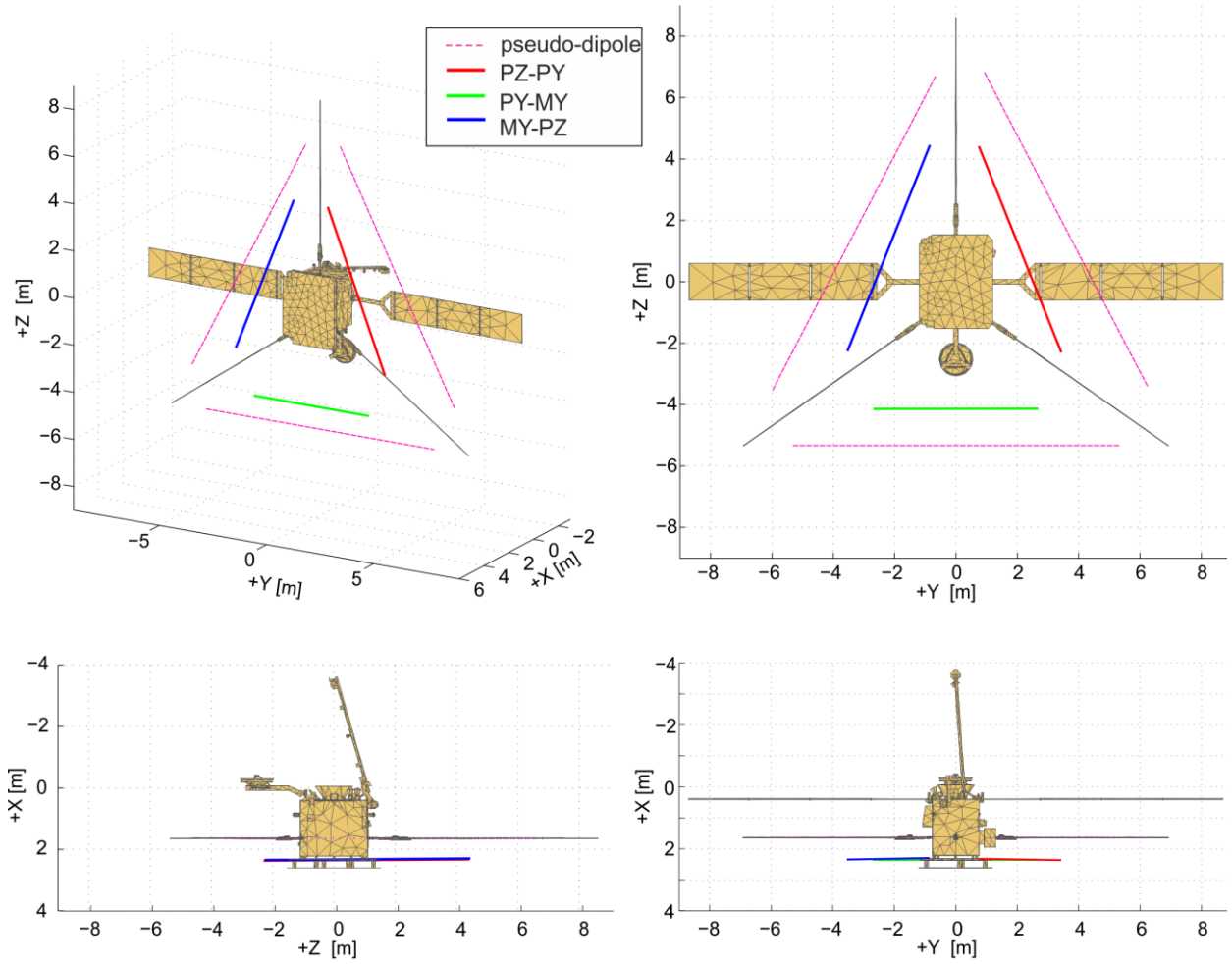

Figure 7. Effective length vectors at 300 kHz for a dipole configuration. The dipole effective vectors have been calculated from the effective vectors of monopoles. "Pseudo-dipoles" mean the vectors formed by the corresponding monopoles, e.g. pseudo dipoles PZ-PY is obtained from the difference between PZ and PY monopoles. The real monopoles (physical antennas) are given in black.

Figure 6 and 7 show the effective length vectors of the monopoles and dipoles (in color) and the physical position of the real antennas or pseudo-dipoles. The results show that effective lengths vectors of PZ, PY and MY monopoles are offset from the mechanical axes by 9.1°, 13.6° and 13.6° towards the positive X-axis (sunward direction) while the physical antennas are coplanar in the YZ-plane. It was found that the azimuthal angles of the effective axes are not altered by the presence of the spacecraft structure. The effective lengths of the PZ, PY and MY antenna are 4.41 m, 3.91 m and 3.91 m correspondingly. These lengths are smaller than length of the antenna rods (6.5 m). The effective vectors of the dipoles are practically coplanar in the YZ-plane. The offset is about 1°. Two dipoles PZ-PY and MY-PZ have a small offset by 5.6° from the pseudo dipoles as calculated from the monopoles.

Table 3 shows the calculated open port capacitance matrix for the monopoles. To verify the validity of the simulation results, the obtained antenna capacitances (Table 3) can be compared with theoretical estimations (e.g. Macher and Oswald, 2011):

$$C = \frac{2\pi\varepsilon_0 l_A}{\ln\left(\frac{2l_A}{d}\right)-1} \qquad (3)$$

where l_A is the antenna length, d *is* the diameter of the antenna and ε_0 is the permittivity of free space. For monopole antenna with l_A=6.5 m and the averaged diameter is d=0.0255 m the antenna capacitance after the equation (3) is 69.1 pF. This is comparable to the simulation result presented in table 3, where the antenna capacitances are 71.6 - 72.9 pF. The small difference between theoretical estimations and the simulations can be explained that, in fact, the RPW monopole is a cone with a base diameter of 3.2 cm and a tip diameter of 1.9 cm while the equation (3) is for cylindrical antennas.

Table 3. Antenna system capacitance matrix Ca for monopoles

	Capacitance matrix (open port, pF)		
	PZ	**PY**	**MY**
PZ	71.6	-3.3	-3.3
PY	-3.3	72.9	-3.4
MY	-3.3	-3.4	72.9

3.2.2 Loaded ports

The calculation was done also for loaded ports. According to the information from PI of RPW Dr. M. Maksimovic (LESIA, France) the base (or stray) capacitance of each RPW antennas including receiver input, cables, and antenna mounting is 103 pF. Generally, the loads at the ports can be represented by a local impedance matrix Z_L. The effect on the transfer matrix T is given by (Macher et al., 2007)

$$\boldsymbol{T} = (\mathbf{1} + \boldsymbol{Z}_A \boldsymbol{Z}_L^{-1})^{-1} \boldsymbol{T}^O = (\mathbf{1} + \boldsymbol{C}_A^{-1} \boldsymbol{C}_L)^{-1} \boldsymbol{T}^O \qquad (4)$$

where $\boldsymbol{Z}_A$ and $\boldsymbol{C}_A$ are the antenna impedance and capacitance matrices (Table 2) and $\boldsymbol{T}^O$ is the open port transfer matrix which contains the open port effective length vectors as rows. The expression on the right is valid in the quasi-static frequency range. The load capacitance matrix $\boldsymbol{C}_L$ contains the base capacitances in its diagonal.

The effective antenna vectors for loaded ports are presented in Table 4. Table 5 shows the effective antenna vectors for open and loaded ports.

Table 4. Fffective length vectors of PZ, PY and MY monopoles and PZ-PY, PY-MY and MY-PZ dipoles compared with physical position of the RPW antennas for loaded ports. The calculation was done for loaded ports with total base capacitance 103 pF.

ANT	Mechanical antennas			Effective antenna vectors			
	h, m	θ, deg	φ, deg	h_e, m	θ, deg	φ, deg	γ, deg
PZ	6.5	0.0	0.0	1.86	8.3	-0.4	8.3
PY	6.5	125	90	1.65	132.1	76.4	12.9
MY	6.5	125	-90	1.65	132.0	-76.3	12.9
Dip. PZ-PY	11.53	152.5	90	3.18	158.0	89.0	5.6
Dip. PY-MY	10.65	90.0	90	2.38	90.0	90.0	0.0
Dip. MY-PZ	11.53	152.5	-90	3.18	158.1	-88.9	5.6

Table 5. Effective length vectors for open port vs loaded ports.

ANT	Open ports				Loaded ports			
	h_e, m	θ, deg	φ, deg	γ, deg	h_e, m	θ, deg	φ, deg	γ, deg
PZ	4.41	9.1	-0.4	9.1	1.86	8.3	-0.4	8.3
PY	3.91	132.2	75.2	13.6	1.65	132.1	76.4	12.9
MY	3.91	132.3	-75.2	13.6	1.65	132.0	-76.3	12.9
Dip. PZ-PY	7.53	158.1	89.0	5.6	3.18	158.0	89.0	5.6
Dip. PY-MY	5.60	90.00	90.0	0.0	2.38	90.0	90.0	0.0
Dip. MY-PZ	7.53	158.2	-89.1	5.6	3.18	158.1	-88.9	5.6

3.2.3 Far-field directivity in a quasi-static range

The far-field directivity pattern of the RPW antennas in a quasi-static range have smooth toroidal shape (Fig. 8) while for higher frequencies this shape is complex, as presented in the section 3.5

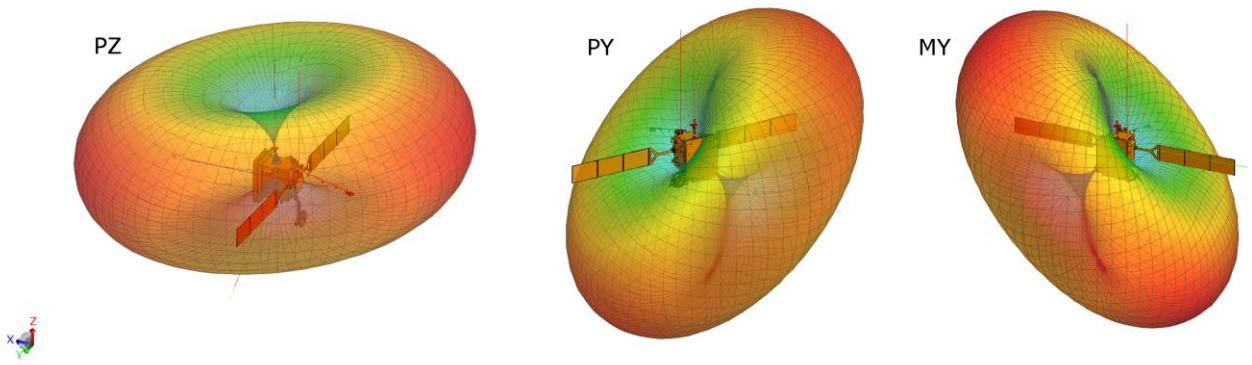

Figure 8. Far-field directivity pattern of the PZ, PY and MY antennas at 300 kHz.

3.3 Thermal antenna bending.

The another important task was to study the offset of effective axes due to a thermal antenna bend which will occur when the antennas are heated by solar radiation. The flight path of the spacecraft is planned to be quite near to the Sun, where the solar radiation is high. Due to the attitude of the spacecraft, which is controlled in a way that the positive x-axis always faces toward the Sun, one side of each antennas will always face the Sun, while the other side will always be in the shadow. It is expected that there will be a large temperature gradient as result of the uneven illumination, which, in turn will result in a thermal bending effect, which bends the antennas away from the Sun. This bending effect will result in differently shaped antennas, so the antenna properties will be different compared to straight antennas. The thermal bend estimated by CNES engineers can be more than 1.2 m at the distance of 0.22 AU from the Sun.

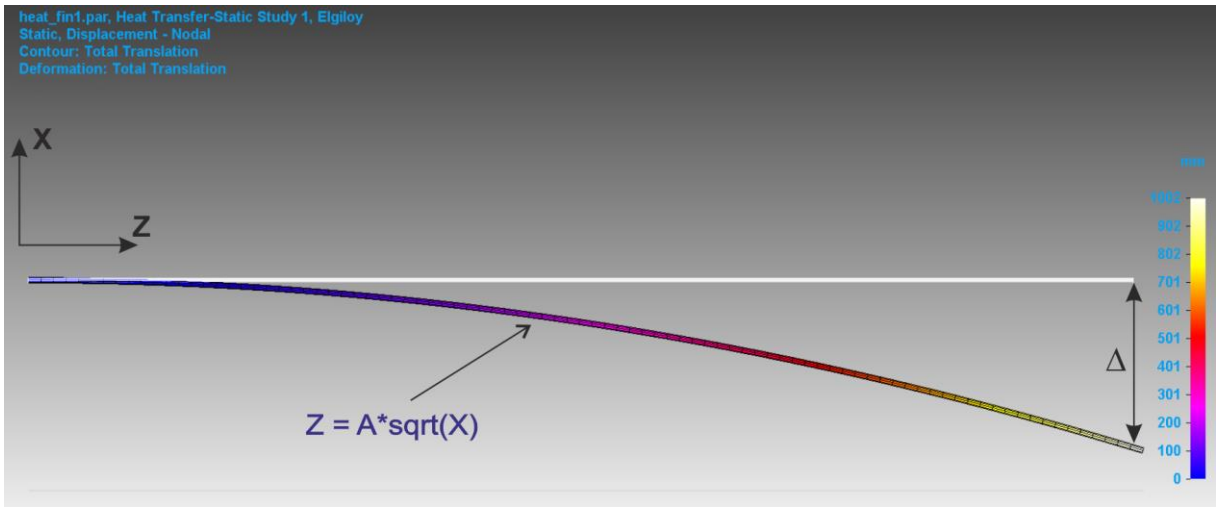

Figure 9. Bending of an unevenly heated cylindrical metallic (elgiloy) antenna. Δ shows offset of the antennas tip. Displacement of the deformed antenna stroke is coded by color. The shape of the bended antenna in XZ plane can be approximated as $Z = A\sqrt{X}$, where the coefficient A depends on the heat flux due to solar radiation.

Using a thermal simulation tool in Solid Edge CAD software we have simulated the bending of the unevenly heated metallic tube. *It is important to note, that we did not model the real bending of the spacecraft antenna depending on the solar irradiation because it requires a complicated thermal analysis with taking into account thermal properties of all spacecraft structures.* Such thermal analysis will be done by the spacecraft developer after finalization of the spacecraft design.

Our simple simulations have shown that the unevenly heated antenna rod will be bended as shown in Figure 9. The bend, of course, depends on the solar heat flux which will be different in each parts of the spacecraft orbit. In the example shown in Figure 10 the offset (Δ) of the antenna tip is 1 m that corresponds to the situation when the spacecraft will be close to the Sun. So, by varying the heat flux we have defined the shape of the bended antennas for different offsets of the

antenna tip (Δ), from Δ=10 cm to Δ=150cm. *The thermal longitudinal extension of the antenna was not taking into account*. It was found that the shape of the bended antenna in XZ plane can be described as: $Z = A\sqrt{X}$ where A is a coefficient which depends on the heat flux and Z and X is the coordinates in XZ plane. Our simplified thermal simulations have shown that coefficient A can be approximated by the equation: A=-0.46818+6.86918*$\Delta^{-0.4855}$ where Δ is the offset of the antenna tip.

In this way, we have designed 15 models of the Solar Orbiter with the different thermal bends, i.e. from 10 cm to 150 cm. Then, we have studied the influence of the thermal bending of the antennas on resulting effective antenna length vectors in the same way as it was done for the initial spacecraft configuration (with undeformed antennas) i.e. each model has been imported to the CADFEKO and the currents distributions have been simulated by FEKO. The results of the simulations are presented in Table 6 and Fig. 11.

As shown in the Table 6 the tilt of the effective length vector is decreased from 9.1°,13.6°,13.6° (initial configuration without bending) up to 3.9°, 9.9° and 9.9° for the Δ = 1.5 m. The decreasing of the effective length (h_e) is small from 4.41 to 4.37 m for PZ antenna and from 3.91 to 3.83 for PY and MY antennas. *In fact, our results for the effective length h are not fully correct, because we did not account the longitudinal thermal extension of the antennas, which can be significant when the spacecraft will be close to the Sun.* The correct (h_e) can be calculated only after future complete thermal analysis of the Solar Orbiter by the spacecraft developer. Therefore, in the Fig. 11 we show only changes of the angular separation (γ) between effective antenna vector and real antenna rod. Since the thermal bend of the antenna varies with the distance of the spacecraft to the Sun our results can be used for the determination of the effective antenna properties in different orbital phases of the Solar Orbiter mission.

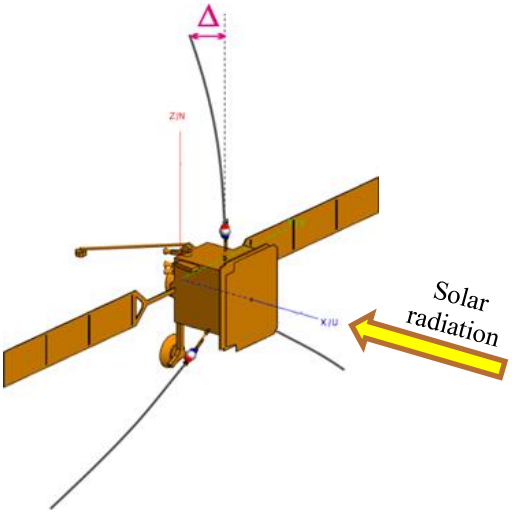

Figure 10. Solar Orbiter model with thermal bended antennas. Δ indicates the offset of each antenna tip.

Table 6. The effective antenna vectors for different thermal bends (Δ) of the antennas.

Tip offset	Effective antenna vectors											
	PZ				PY				MY			
Δ, m	h_e, m	θ, deg	φ, deg	γ, deg	h_e, m	θ, deg	φ, deg	γ, deg	h_e, m	θ, deg	φ, deg	γ, deg
0.0	4.41	9.1	-0.4	9.1	3.91	132.3	75.2	13.6	3.91	132.2	-75.2	13.6
0.1	4.41	8.7	-0.4	8.7	3.91	132.3	75.8	13.3	3.91	132.3	-75.8	13.2
0.2	4.41	8.4	-0.4	8.4	3.91	132.4	76.3	13.0	3.91	132.4	-76.2	13.0
0.3	4.41	8.1	-0.5	8.1	3.9	132.5	76.7	12.7	3.9	132.4	-76.7	12.7
0.4	4.4	7.7	-0.5	7.7	3.89	132.6	77.2	12.5	3.89	132.5	-77.2	12.5
0.5	4.4	7.4	-0.5	7.4	3.88	132.7	77.7	12.2	3.89	132.6	-77.7	12.2
0.6	4.39	7.0	-0.5	7.0	3.87	132.7	78.2	12.0	3.88	132.7	-78.2	11.9
0.7	4.38	6.7	-0.5	6.7	3.86	132.8	78.8	11.7	3.87	132.7	-78.7	11.7
0.8	4.38	6.4	-0.6	6.4	3.86	132.9	79.3	11.5	3.86	132.8	-79.3	11.4
0.9	4.37	6.0	-0.6	6.0	3.85	133.0	79.8	11.2	3.86	132.9	-79.8	11.2
1.0	4.37	5.7	-0.6	5.7	3.85	133.0	80.3	11.0	3.85	133.0	-80.3	10.9
1.1	4.37	5.3	-0.7	5.3	3.84	133.1	80.9	10.7	3.85	133.0	-80.8	10.7
1.2	4.37	5.0	-0.7	5.0	3.84	133.1	81.4	10.5	3.84	133.1	-81.4	10.5
1.3	4.37	4.6	-0.8	4.6	3.84	133.2	82.0	10.3	3.84	133.1	-81.9	10.2
1.4	4.37	4.2	-0.9	4.2	3.83	133.2	82.5	10.1	3.84	133.2	-82.5	10.0
1.5	4.37	3.9	-0.9	3.9	3.83	133.3	83.1	9.9	3.83	133.2	-83.1	9.8

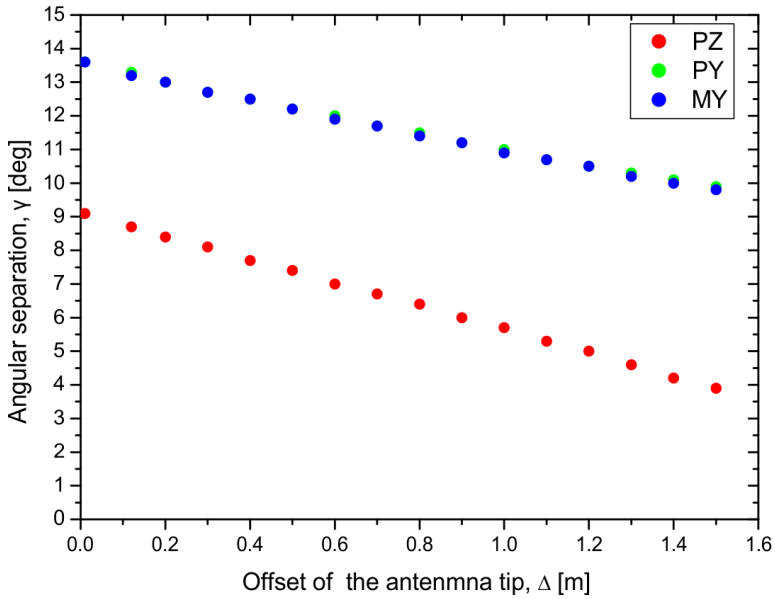

Figure 11. Result of the numerical simulations of the reception properties of the thermal bended RPW antennas. The dependence of the angular separation γ between the effective antenna vector and the real antenna rods is shown for different offsets of the antenna tip Δ. The colors indicate PZ, PY and MY antennas.

3.4 Dependence on the solar panel orientation.

We have also simulated the antenna reception properties for different position of the rotatable solar panels. The panels can be turned up to 45 deg. out of the vertical position (Fig. 12) during different phases of the spacecraft mission. *Our simulations showed no significant influences of the solar panel rotation on the resulting effective antenna vectors.*

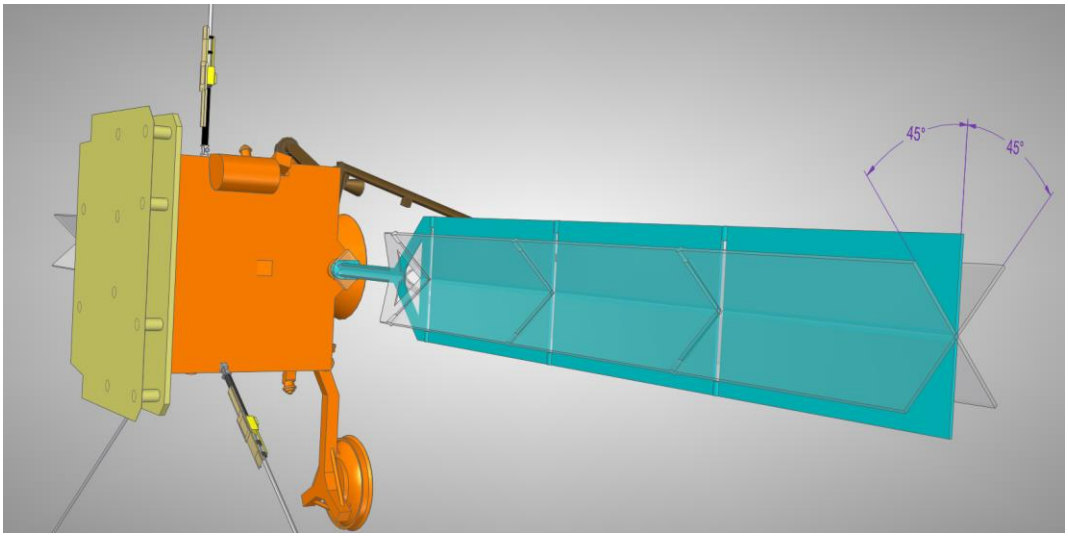

Figure 12. Solar Orbiter CAD model with different position of the solar panels. During different phases of the spacecraft solar panels can be turned up to 45 deg. out of the vertical position.

3.5 High-frequency characteristics

The directivity patterns and the impedances of the antenna have been also simulated up to frequencies of 16 MHz. Far-field directivity patterns (Fig. 13) have smooth toroidal shape from quasi-static range up to ~9 MHz where the first local resonance frequency is reached at ~9.2 MHz when an imaginary part of the antenna impedance turns from positive values to negative ones in a zero crossing (Fig. 14). Than for the higher frequencies the patterns are strongly frequency dependent. It has a complex shape with several lobes as the patterns. The impedance diagrams for PZ, Py and MY anennas are shown in Fig. 14.

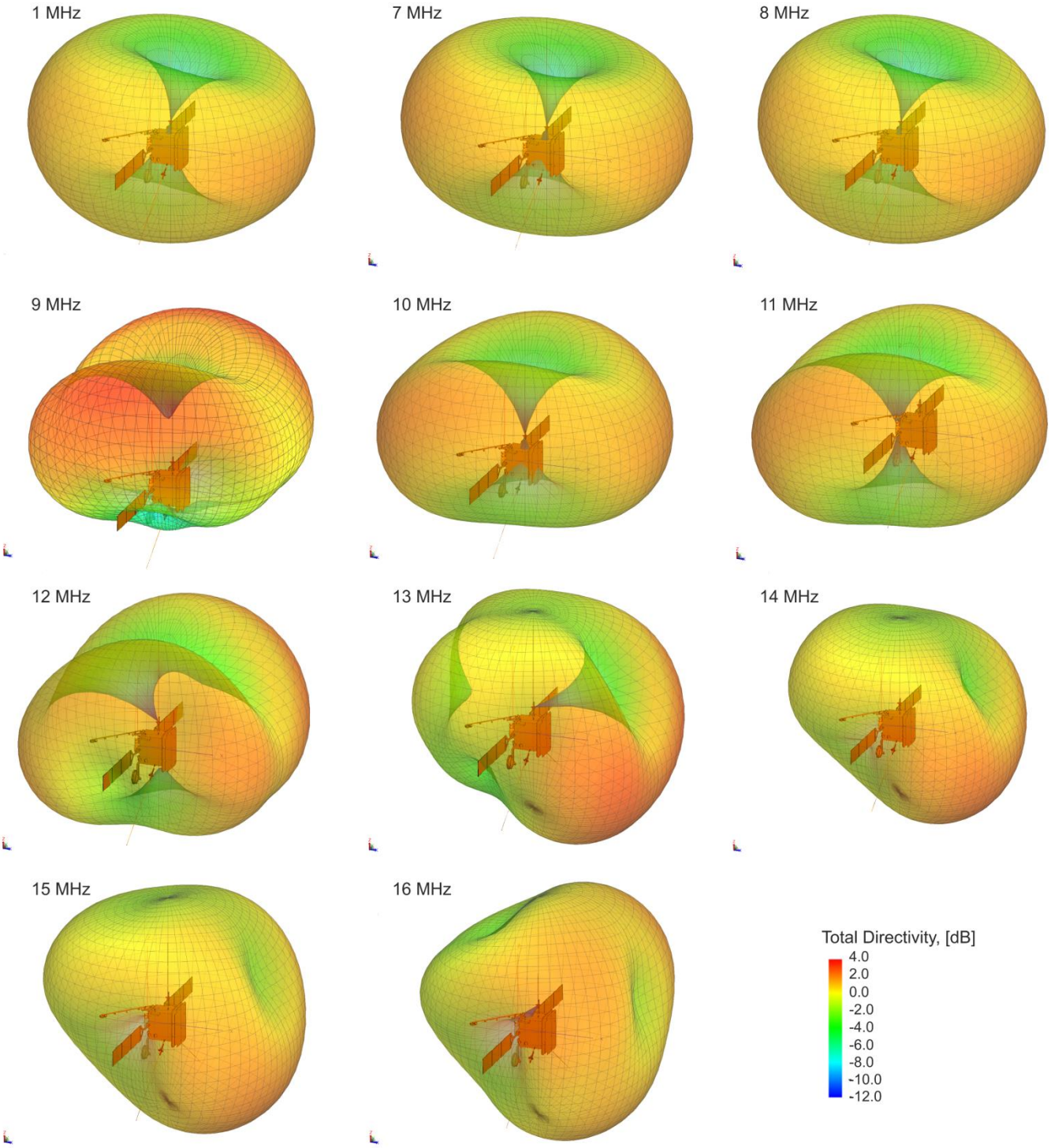

Figure 13. Far-field directivity patterns of **PZ** antenna for frequency range 1MHz – 16 MHz. Color coding (in dB) indicates the total directivity.

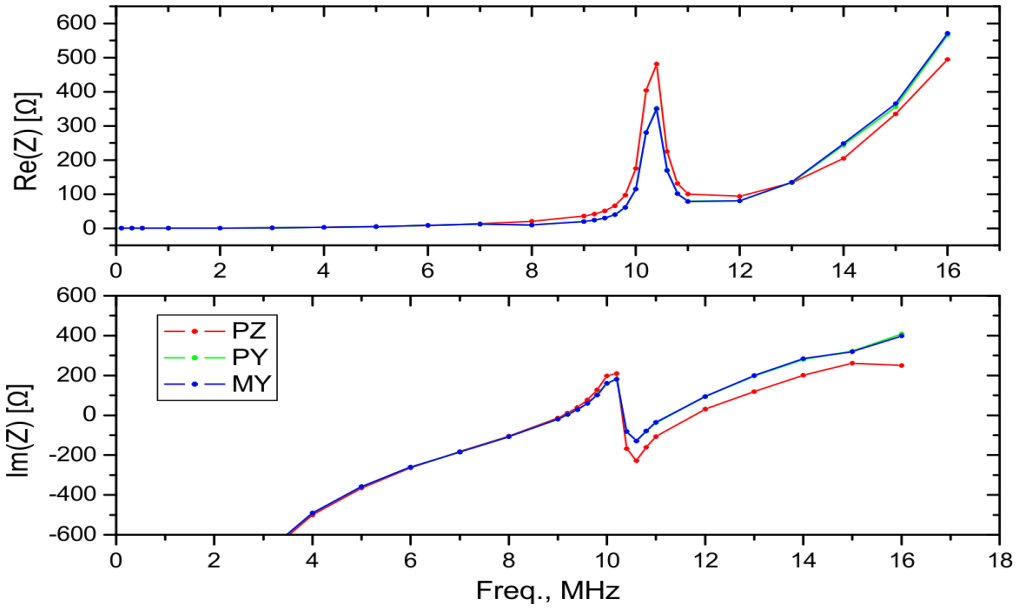

Figure 14. The frequency dependent antenna impedances. Antenna resonance an ~10.3 MHz is clearly seen, when the imaginary part of the impedance has a zero crossing.

4. Rheometry measurements

The Rheometry measurements were performed using the existing 1:50 scaled gold platted model of the Solar Orbiter (see Fig. 16) which was developed in the frame of the ESA funded project “Anechoic chamber measurements of spaceborne antennas” (2012-2013). The model is loaned to IWF (Space Research Institute) on base on Loan Agreement between IWF and ESA. This model was built in 2012 and the antenna system consisted of a set of three identical antenna monopoles 5 m length. Due to technical reasons Solar Orbiter / RPW team changed the antenna design in 2013. The new RPW antenna system consists of a set of three identical monopoles (6.5 m length) deployed from two corners and one side of the spacecraft. Therefore the first task was to adopt the existing spacecraft model to the correct antenna lengths. The design of new antennas is shown in the Figure 1c. The antenna system consists of boom, deploying mechanism and 6.5 m length antenna stroke. Additionally, there are thermal shields in form of niobium plates. Of course, such design cannot be modeled in scale 1:50, especially deploying mechanism and thermal shields. Therefore, we have simplified the model of antennas (see Fig. 15). The antenna length in the scaled model is 130 mm, which corresponds to 6.5 meters of real antenna. The boom is 19.7 mm lengths measured from the spacecraft body. The boom and antenna is connected by the 10 mm plastic (isolator) connector.

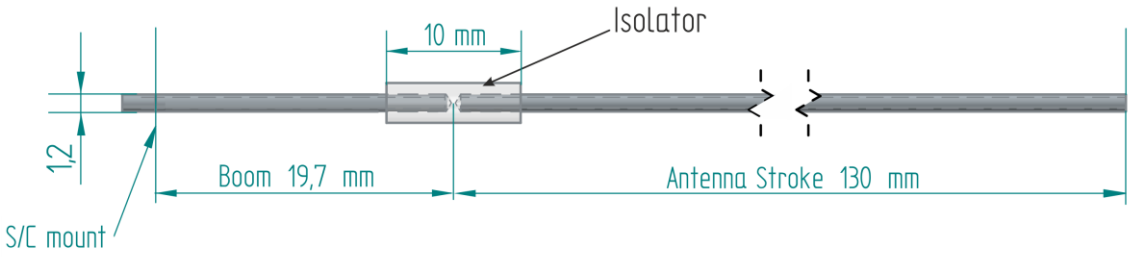

Figure 15. RPW antennas for the rheometry experiment. The left part shows the antenna boom with a length of 19.7 mm, and an outer diameter of 1.2 mm. The right part shows the antenna stroke with a length of 130 mm. The boom and the antenna stroke are separated by a polyamide plastic isolator. The antennas are coated with gold.

As was mentioned in the Introduction, the method of the rheometry is based on electrolytic tank measurements where the scaled gold plated model is immersed in a water-filled with homogeneous electric field. The model rotates with regard to direction of the electric field in the tank and the effective antenna vectors and the antenna capacitance matrix can be defined in the *quasi-static frequency range*. The Solar Orbiter model could rotate around two different suspension axes. Details of the setup and the measurement principle are explained in Rucker et al., 1996 and Macher et al., 2007. The respective measurements are shown in Fig. 16.

The results are given in Table 7, where the open port effective length vectors are compared with the respective physical antenna lengths and directions. The table also includes the results for dipole configuration of the antennas. The results also take into account the 10 pF base capacitance representing shielding at a gap and assuming 25 mm antenna diameter (real antenna has conical shape). Similar to the numerical simulations the effective length vectors h_e for dipoles have been calculated by subtracting the effective vectors of corresponding monopoles (see section 3.2.1). The capacitance matrix of monopoles is displayed in Table 8. Using the total base capacitance in 103 pF we have also defined the effective length vectors for loaded ports, as shown in Table 9. The results of the rheometry measurements and numerical simulations for open and load ports are compared in Table 10 and 11.

Table 7. Results of the rheometry measurements for open port. Effective length vectors of PZ, PY and MY monopoles and PZ-PY, PY-MY and MY-PZ dipoles compared with physical position of the RPW antennas. h is antenna length, θ is colatitude and φ is azimuth angle. The angle γ is the angular separation between effective antenna vector and real antenna rod. The dipole effective vectors have been calculated from effective vector of the monopoles. The results take into account the 10 pF base capacitance representing shielding at gap and assuming 25 mm antenna diameter.

ANT	Mechanical antennas			Effective antenna vectors			
	h, m	θ, deg	φ, deg	h_e, m	θ, deg	φ, deg	γ, deg
PZ	6.5	0.0	0.0	4.58	8.4	-5.1	8.4
PY	6.5	125	90	4.12	132.8	75.0	14.1
MY	6.5	125	-90	4.15	133.5	-75.9	13.8
	Pseudo dipoles			Effective vectors of dipoles			
Dip. PZ-PY	11.53	152.5	90	7.91	157.9	87.8	5.5
Dip. PY-MY	10.65	90.0	90	5.89	90.0	89.6	0.4
Dip. MY-PZ	11.53	152.5	-90	7.89	158.4	-88.4	5.9

Table 8. Rheometry measurements of antenna system capacitance matrix Ca for monopoles. The additional 10 pF base capacitance representing shielding at gap has been added to the self-capacity (diagonal elements).

	Capacitance matrix (open port, pF)		
	PZ	**PY**	**MY**
PZ	68.8	-6.7	-6.9
PY	-6.7	70.4	-7.2
MY	-6.9	-7.2	72.1

Table 9. Results of the rheometry measurements for loaded ports. The calculation was done for total base capacitance 103 pF.

ANT	Mechanical antennas			Effective antenna vectors			
	h, m	θ, deg	φ, deg	h_e, m	θ, deg	φ, deg	γ, deg
PZ	6.5	0.0	0.0	1.94	7.6	-5.3	7.6
PY	6.5	125	90	1.74	132.6	76.1	13.2
MY	6.5	125	-90	1.75	132.3	-77.0	12.5
Dip. PZ-PY	11.53	152.5	90	3.35	157.7	87.7	5.3
Dip. PY-MY	10.65	90.0	90	2.51	89.9	89.6	0.4
Dip. MY-PZ	11.53	152.5	-90	3.34	158.2	-88.3	5.8

Table 10. Fffective length vectors obtained from numerical simulations and rheometry measurements for open ports.

ANT	Numerical simualtions				Rheometry measurements			
	h_e, m	θ, deg	φ, deg	γ, deg	h_e, m	θ, deg	φ, deg	γ, deg
PZ	4.41	9.1	-0.4	9.1	4.58	8.4	-5.1	8.4
PY	3.91	132.2	75.2	13.6	4.12	132.8	75.0	14.1
MY	3.91	132.3	-75.2	13.6	4.15	133.5	-75.9	13.8
Dip. PZ-PY	7.53	158.1	89.0	5.6	7.91	157.9	87.8	5.5
Dip. PY-MY	5.60	90.00	90.0	0.0	5.89	90.0	89.6	0.4
Dip. MY-PZ	7.53	158.2	-89.1	5.6	7.89	158.4	-88.4	5.9

Table 11. The same as in Table 10 but for loaded ports with base capacitance 103 pF.

ANT	Numerical simualtions				Rheometry measurements			
	h_e, m	θ, deg	φ, deg	γ, deg	h_e, m	θ, deg	φ, deg	γ, deg
PZ	1.86	8.3	-0.4	8.3	1.94	7.6	-5.3	7.6
PY	1.65	132.1	76.4	12.9	1.74	132.6	76.1	13.2
MY	1.65	132.0	-76.3	12.9	1.75	132.3	-77.0	12.5
Dip. PZ-PY	3.18	158.0	89.0	5.6	3.35	157.7	87.7	5.3
Dip. PY-MY	2.38	90.0	90.0	0.0	2.51	89.9	89.6	0.4
Dip. MY-PZ	3.18	158.1	-88.9	5.6	3.34	158.2	-88.3	5.8

The effective lengths vectors of Pz, Py and My antennas are offset from the mechanical axes by 8.4°, 14.1° and 13.8° towards the positive x-axis (the physical antennas are coplanar in the YZ-plane). The effective lengths of the Pz, Py and My antenna are 4.58m, 4.12m and 4.15m correspondingly. The obtained values are in a good agreement with the numerical calculations. The errors in the rheometry measurements are about 1° for the angles. There is only difference is

in the obtained antenna lengths. In particular, the effective antenna lengths from the numerical simulations are 4.41m, 3.91m and 3.91m, that is about 4-5% shorter than lengths from the rheometry measurements. The reason of this difference, that the real antenna is mounted on the 1 m boom with metallic thermal shield and, therefore, the part of each antenna (0.42m) is partially in the shadow of these conductive thermal shields. These shields can be regarded as a Faraday cage for 0.42m of the antenna and, in fact, the effective length of such antennas is shorter. Due to small size of the scaled model it was not possible to reproduce these thermal shields in the hardware spacecraft model. Therefore the effective antenna length in numerical simulation, which includes thermal shields, is shorter than the effective lengths obtained from the rheometry measurements.

The other discrepancy is the azimuthal angle φ for PZ antenna. The rheometry measurements gave $\varphi = 5.1°$ while in the numerical simulation $\varphi = -0.4°$. This difference it is due to the fact that the Solar Orbiter model which was used for the rheometry measurements has only 2 rotation axes, i.e. around Z_{sc} and X_{sc} spacecraft axes. Therefore, PZ antenna was either parallel or perpendicular to the rotation axes. In this situation it was difficult to define precisely the azimuthal tilt φ of the PZ antenna. Therefore, the result of numerical simulations ($\varphi = -0.4°$) is more plausible. Nevertheless, this discrepancy has no influence on the angular separation γ while azimuthal angle φ is calculated from the projection of the PZ effective antenna vector on the XY plane and this projection is small ($\propto \sin 8.4° = 0.14$). The results for the angular antenna separations out of the rheometry measurements and the numerical simulations are similar, i.e. $\gamma = 8.4°$ (rheometry) and $\gamma = 9.1°$ (numerical simulations).

Figure 16. Rheometry measurements of the RPW antennas in a water tank. The top panels show the gold plated Solar Orbiter model.

5. Accuracy estimation of the in-flight calibration of the RPW antennas.

One of the methods of the determination of the real reception properties of the spaceborne antennas is an in-flight calibration in which the effective antenna length vectors can be investigated by analyzing the temporal variation of the intensity of the radio emission emitted from the point radio source with known location. Terrestrial Auroral kilometric radiation (AKR) can be used as radio source for the in-flight antenna calibration. The methodology of this calibration is well described in Vogl et al. [2004] and has been applied for e.g., ISEE-3 [Fainberg et al., 1985], Voyager [Wang and Carr, 1994], Interball-2/Polrad [Panchenko, 2004], Cassini [Vogl et al., 2004; Cecconi and Zarka, 2005] and STEREO/WAVES [Panchenko, 2014]. In order to perform the in-flight calibration with good accuracy spaceborne antennas must rotate with respect to the direction of the radio source.

Several spacecraft roll maneuvers are scheduled in the early stage of the Solar Orbiter mission. During each maneuver the Solar Orbiter will rotate around X axis (directed towards the Sun) during 8 hours with angular speed 0.05 or 0.1 degrees per second. The series of 8-hours lasting roll maneuvers per day are scheduled for the following intervals of time:

1. 12 – 26 Oct., 2018
2. 15 – 27 Feb., 2020
3. 05 – 17 Dec., 2021

We have estimated the accuracy of the planned in-flight calibration in order to show which scheduled roll maneuvers can be effectively used for determination of the RPW antenna properties. The main idea is to estimate how accurate the antenna directivity, i.e., the directions and length of the antenna effective vectors can be derived, depending on the position of the spacecraft relative to AKR sources as well as signal to noise ratio. Taking into account the similarity of the Solar Orbiter/RPW and STEREO/WAVES instruments we have applied the same methods as have been used for the in-flight calibration of the STEREO/WAVES antenna [see Panchenko et al., 2014]. The positions of the RPW antenna effective length vectors in the spacecraft frame are shown in Figure 1.

5.1 Visibility of the AKR sources.

First, we have estimated on which parts of the Solar Orbiter trajectory (when the roll maneuvers are scheduled) the AKR sources can be observed. As was shown in the several studies, e.g. Hanasz et al. [2003], the AKR is mainly observed in the nightside part of the terrestrial magnetosphere. A bulk of its occurrence frequency distribution was concentrated in the evening sector with a peak near 21 - 22 h of magnetic local time (MLT) and 70° invariant latitude. Therefore, for our estimation we assumed that the AKR sources are spread located in the region of MLT between 19 - 23 h and invariant latitudes between 65° - 75°.

For the estimation of the visibility of the AKR sources we used a simple geometrical model of the

AKR source visibility with a straight-line propagation of the radio emission. In the model the sources of the AKR have been located in the region of 19 - 23 h of MLT and 65° - 75° of invariant latitudes at altitudes corresponds to the 300 kHz – peak of AKR spectral density. The AKR observations have also shown that after source escaping the R-X mode of AKR is propagated in angles ~70 – 90 degrees relative to the local magnetic field (e.g. Bahnsen et al., 1987; Louarn and Le Qu´eau, 1996). Therefore, in our calculations we have assumed that AKR beam is a filled cone with half-open angle of α=70° relative to the local magnetic field line.

For a given position of the spacecraft and the AKR source we have calculated the angle β between vector of magnetic field in the positions of the AKR sources and the vector of direction from the spacecraft position to the AKR source. When the angle $\beta > 180° - \alpha$ (for Northern hemisphere) and $\beta < \alpha$ (for Southern hemisphere) than the spacecraft is inside of the AKR beam and therefore, this AKR source can be visible from the given spacecraft position. The probability of the AKR observation for each position of the spacecraft is calculated as relation between number of visible AKR sources to the number of all modeled AKR sources in the region 19 – 23 h MLT and 65° – 75° invariant latitudes (the sources were placed at each 1/15 h of MLT and 1° of invariant latitudes). The results are presented in Figure 17. Panel (a) shows the trajectory of the Solar Orbiter in GSE coordinates during the first scheduled roll maneuvers on 12 – 26 Oct., 2018. Panels (b) and (c) show the calculated probability of the observation of the Northern and Southern AKR sources in different part of the orbit. The probability is coded by a color. The panels (d), (e), (f) and (g), (h), (i) show the trajectory and probability of AKR observation for the roll maneuvers on 15 – 27 Feb., 2020 and 05 – 17 Dec., 2021. As shown on panels (e), (f) and (h), (i) the AKR sources cannot be observed when spacecraft will be at the dayside part of the orbit (21 – 27 Feb., 2020 and 5 – 11 Dec., 2021). In the same time, during other periods of times, i. e. on 12 – 26 Oct., 2018, 15 – 20 Feb., 2020 and 12 – 17 Dec., 2021 the Solar Orbiter will able to detect the AKR from the Northern or Southern hemispheres and, therefore, these observations can be used for in-flight calibration of the RPW antennas.

5.2 Simulation of the in-flight calibration of the RPW antennas.

We have modeled the in-flight calibration using the same methods which have been applied for STEREO/WAVES antennas reported in [Panchenko et al., 2014].

The main idea of simulation of the in-flight calibration procedure and errors estimation involves:

- Derivation of the model-predicted output voltages at each receiver channel.
- Simulation of the AKR observations.
- Applying of the least squares method combined with a genetic algorithm to fit the model-predicted signals to the simulated AKR observation.
- Errors estimation.

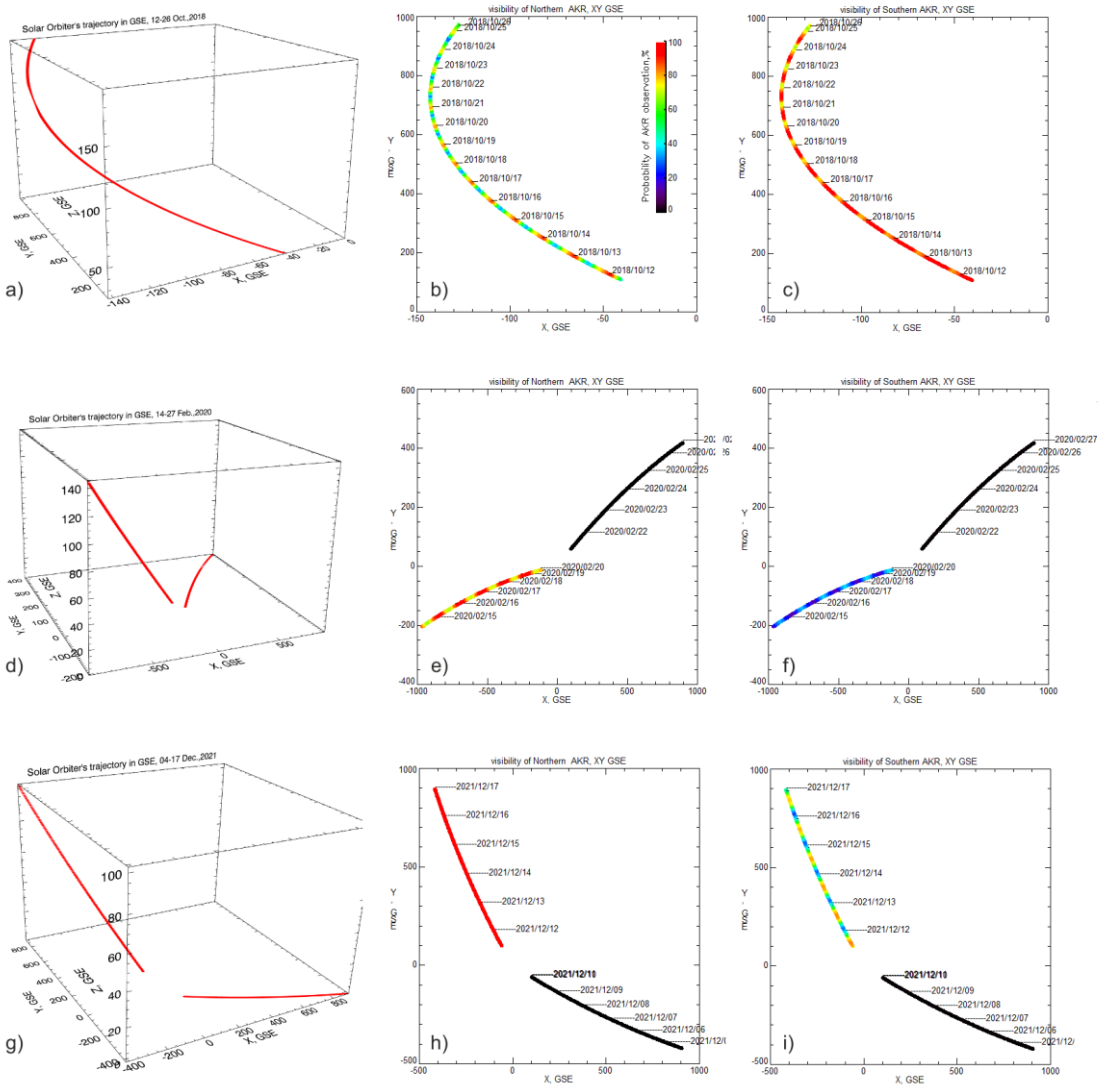

Figure 17. Probability of the AKR observation for different parts of Solar Orbiter trajectory during scheduled roll maneuvers on 12 – 26 Oct., 2018, 15 – 27 Feb., 2020 and 05 – 17 Dec., 2021. Panels (a), (d) and (f) show the spacecraft orbit in GSE coordinates. Panels (b), (e) and (h) represent the probability of AKR observation from Northern sources and panels (c), (f) and (i) from Southern sources along Solar Orbiter trajectory in XY plane. The probability of AKR observation is coded by color.

Derivation of the model-predicted output voltages. Taking into account that the characteristics of the RPW receiver are similar to STEREO/WAVES instrument (Bougeret et al. [2008]) we described the receiver outputs (P_mod) by analytical expressions for each channels of Solar Orbiter/RPW: three auto correlations between each of the two antennas, three real and three imaginary part of cross-correlation between each pairs of the antennas. We used the equations discussed in Ladreiter et al. [1995], Vogl et al. [2004] and Cecconi and Zarka [2005].

Generation of the simulated AKR observations. We used the position of the AKR source, spacecraft position and the effective lengths of the RPW antennas to generate the synthetic data. The effective lengths were taken from the numerical simulations of the RPW antennas for loaded ports, presented in the Table 4. With a distant observation >100 R_E away from the Earth, the AKR radio sources can be assumed as a point source located at the Earth center. The AKR observations (P_obs) were simulated by adding of the Gaussian noise to the model-predicted data (P_mod). The artificial data sets were simulated for different values of signal to noise ratio (SNR) – 1,3, 5,10, 20 and 30 dB above the background level $S_{bkg} = 10^{-16} V^2/Hz$. The possible digitization noise and errors (Cecconi et al., 2004) was not taken into account.

Fitting of the model-predicted data to the simulated ones. The next step was to fit the model-predicted analytic signals (P_mod) to the simulated data sets (P_obs) with different SNR. A least squares method combined with a genetic algorithm was applied to find the effective length vectors of the RPW antennas in the same way as for STEREO/WAVES [Panchenko et al. 2014]. The results of the fitting are shown in Figure 18 and 19. Note that during the roll maneuvers on 15 – 20 Feb., 2020 (Fig. 19) the rotation plane of the RPW antennas will be near to the perpendicular direction to the AKR sources. As result the rotational modulation of the signals on each antenna will be very small and, therefore, the expected errors of determination of the antenna effective length vectors will be significantly higher.

Errors estimation. In order to estimate the fit errors, we used a so-called “quick and dirty” Monte Carlo or bootstrap method [see Panchenko et al. 2014]. The bootstrap method generates the synthetic data sets by randomly resampling with replacing (*Press et al.* [1992, pp. 689–699] for more details). We synthesized M = 300 bootstrapped data sets using the simulated synthetic data and then applied the fitting procedure to each of 300 bootstrapped data sets and finally, the standard errors of the obtained estimators have been determined.

Results. Figure 20 shows the errors in determination of the effective length vectors $(\Delta\theta, \Delta\varphi, \Delta h)$ of the MY antenna (see Fig. 1) for different values of SNR =1, 3, 5, 10, 20, and 30 dB. The errors have been estimated for 12 Oct. and 15 Oct, 2018 (first scheduled roll maneuvers interval in 2018, when AKR will be visible), 15 Feb., and 20 Feb., 2020 (second roll maneuvers interval) and 13 Dec. and 17 Dec., 2021 (third roll maneuvers interval). As expected, the errors strongly depend on the signal to noise ratio (SNR). For the first and third roll maneuvers interval the errors became less than 1 degree for the angles and 1% for the antenna height when the simulated AKR intensity has SNR > 10 dB. The situation is different for the second roll maneuvers interval in year 2020. In Feb., 2020 the Solar Orbiter will be located relative to Earth in such position, that its rotation plane will be faced towards the AKR sources and, therefore, the all three RPW antennas will rotate in plane nearly perpendicular to the source direction. As result the rotation modulations of the observed signal will be very small (see Fig 19) and the errors of determination of effective length

vector will be significantly higher than for the observations in 2018 and 2021, i.e. ~ 3 deg. for angle θ and ~6 deg. for angle φ (panels c and d in Fig.20). The errors for two other antennas PZ and PY are similar to those presented in Fig. 20 for MY antenna.

Conclusions. Solar Orbiter will able to observe AKR during following periods of time: 12 – 26 Oct., 2018, 15 – 20 Feb., 2020 and 12 – 17 Dec., 2021. These periods can be used for the in-flight calibration of RPW antennas. The accurate antenna effective length vectors measurements require SNR > 10 dB. For the scheduled roll maneuvers on 12 – 26 Oct., 2018 and 12 – 17 Dec., 2021 the effective length vectors of RPW antennas can be determined very accurate with accuracy < 1 degree (one sigma error) and 1% errors in antenna height. In the same time, the interval of roll maneuvers on 15 – 20 Feb., 2020 is unfavorable for the in-flight calibration, i.e. the expected errors will be larger than 3-6 deg.

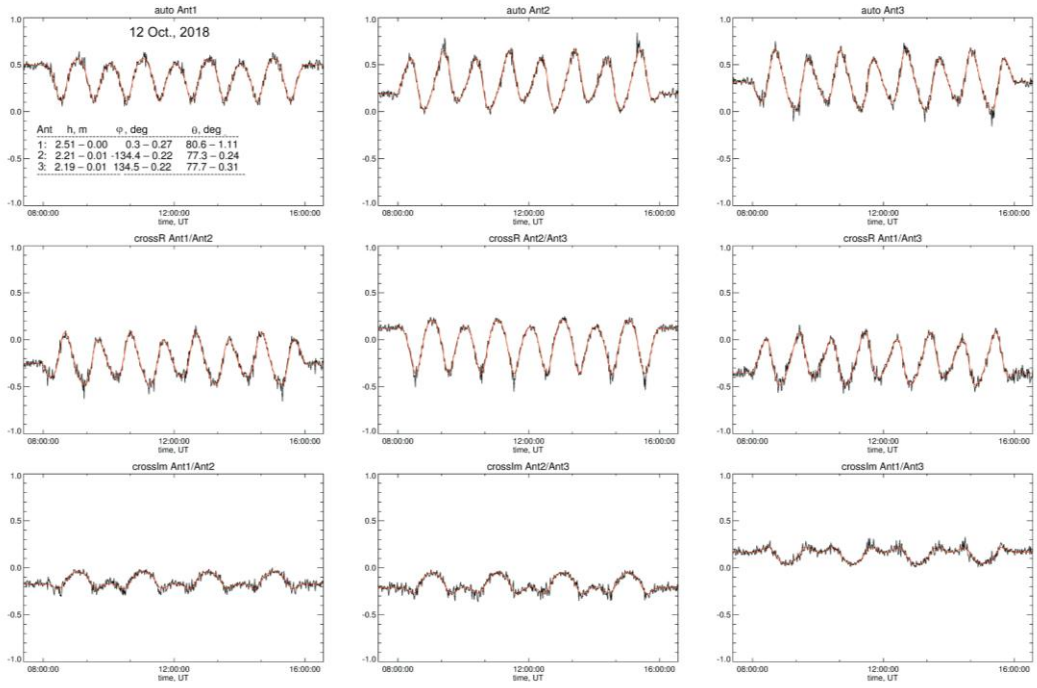

Figure 18. Modeled analytic signals (red lines) fitted to the simulated AKR observations (black line) during Solar Orbiter roll maneuvers on 12 – 26 Oct., 2018. The observations are simulated for the signal/noise ratio SNR=10 dB. The panels show three auto correlations (top panels), three real parts of cross correlations between each of the two antennas (middle panels) and three imaginary parts of cross correlations (bottom panels). Ant1, Ant2 and Ant3 correspond to the PZ, PY and MY monopoles (Fig. 1). The modeled and measured time profiles are normalized by I = Ant1 + Ant2 + Ant3.

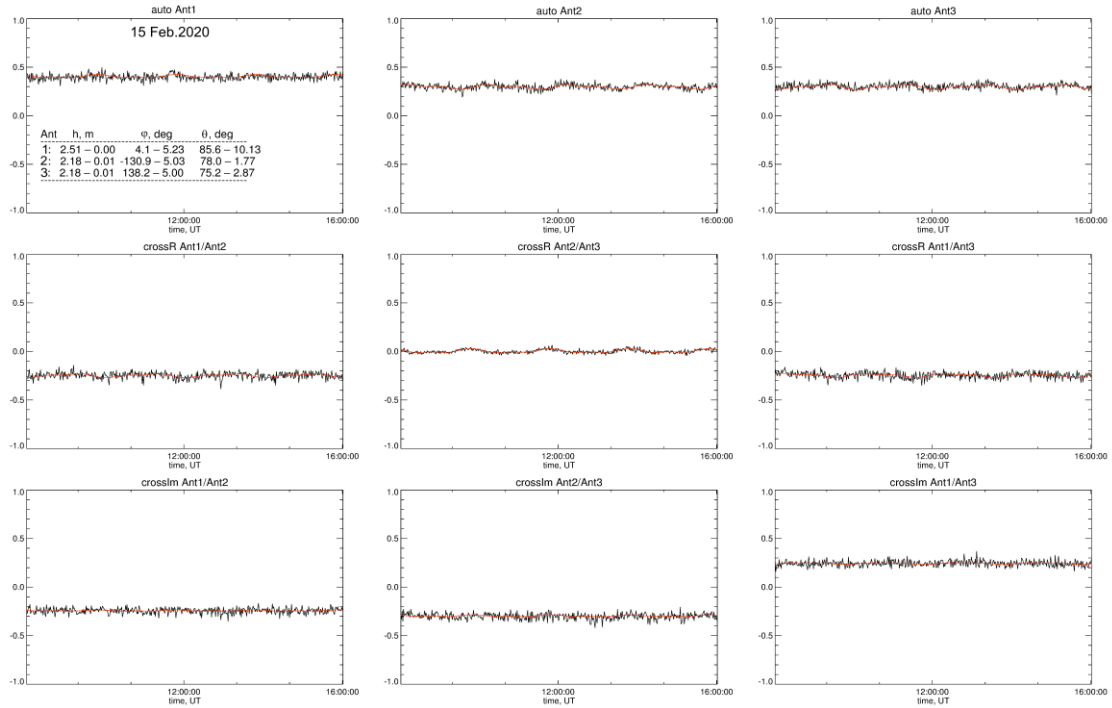

Figure 19. The same as in Figure 3 but for 15 Feb., 2020 and SNR=10 dB.

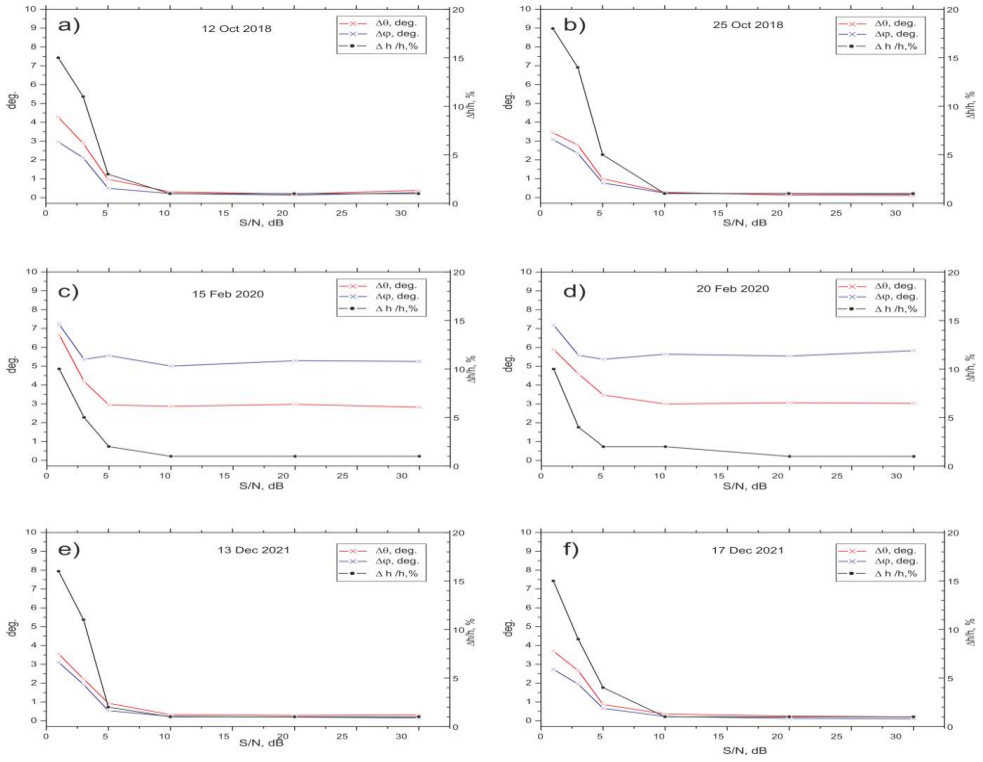

Figure 20. Estimated errors of the determination of the effective length vectors of the MY antenna depending on the signal to noise ratio. Red lines denote errors in determination of the angle $\Delta\theta$, blue lines are $\Delta\varphi$, and black lines (right axes) show the errors in determination of the antenna height h in % relative to Antenna PZ.

6. References

Bahnsen, A. B., M. Jespersen, E. Ungstrup, and I. B. Iversen, Auroral hiss and kilometric radiation measured from the Viking satellite, Geophys. Res. Lett., 14, 471, 1987.

Bougeret, J. L., et al. (2008), S/WAVES: The radio and plasma wave investigation on the STEREO mission, *Space Sci. Rev.*, *136*, 487, doi:10.1007/s11214-007-9298-8.

Cecconi, B., and P. Zarka, Direction finding and antenna calibration through analytical inversion of radio measurements performed using a system of two or three electric dipole antennas on a three-axis stabilized spacecraft, *Radio Sci.*, *40*, RS3003, doi:10.1029/2004RS003070, 2005.

Fainberg, J., S. Hoang, and R. Manning, Measurements of distributed polarized radio sources from spinning spacecraft - Effect of a tilted axial antenna—ISEE-3 application and results, *Astron. Astrophys.*, *153*, 145–150, 1985.

Fischer, G., W. Macher, H.O. Rucker, H.P. Ladreiter, D.F. Vogl and the Cassini/RPWS Team, Wire-grid modelling of Cassini spacecraft for the determination of effective antenna length vectors of the RPWS antennas, In*: Planetary Radio Emissions V*, H.O. Rucker, M.L. Kaiser, Y. Leblanc (Eds.), Austrian Academy of Sciences Press, Vienna, 347-356, 2001.

Hanasz, J., M. Panchenko, H. de Feraudy, R. Schreiber, and M. M. Mogilevsky, Occurrence distributions of the auroral kilometric radiation ordinary and extraordinary wave modes, *J. Geophys. Res.*, *108*(A11), 1408, doi:10.1029/2002JA009579, 2003.

Ladreiter, H. P., P. Zarka, A. Lecacheux, W. Macher, H. O. Rucker, R. Manning, D. A. Gurnett, and W. S. Kurth, Analysis of electromagnetic wave direction finding performed by spaceborne antennas using singular-value decomposition techniques, *Radio Sci.*, *30*, 1699–1712, 1995

Louarn, P., and D. Le Que´au, Generation of the auroral kilometric radiation in plasma cavities - I. Experimental study, Planet. Space Sci., 44, 199, 1996.

Macher, W., and T. Vejda, Design of antenna grid structures. Manual to the MATLAB toolbox. Technical Report of the Space, Research Institute of the Austrian Academy of Sciences, IWF-144, 2003.

Oswald, T.H., W. Macher, G. Fischer, H.O. Rucker, J.L. Bougeret, M. Kaiser, and K. Goetz, Numerical analysis of the stereo waves antennas: first results, *In: Planetary Radio Emissions VI*, H.O. Rucker, W.S. Kurth, and G. Mann (Eds.), Austrian Academy of Sciences, Vienna, 475-482, 2006.

Oswald, T.H., W. Macher, H.O. Rucker, G. Fischer, U. Taubenschuss, J.L. Bougeret, A. Lecacheux, M.L. Kaiser, and K. Goetz, Various methods of calibration of the STEREO/WAVES antennas, *Adv. Space Res.,* 43, 355-364, 2009.

Oswald, T.H., W. Macher, H.O. Rucker, G. Fischer, U. Taubenschuss, J.L. Bougeret, A. Lecacheux, M.L. Kaiser, and K. Goetz, Various methods of calibration of the STEREO/WAVES antennas, *Adv. Space Res.*, **43**, 355-364, 2009.

Panchenko, M., Polarimetry of auroral kilometric radiation with a triaxial nonorthogonal antenna system, *Radio Sci.*, *39*, RS6010, doi:10.1029/2004RS003039, 2004

Panchenko, M., W. Macher, H. O. Rucker,G. Fischer, T. H. Oswald, B. Cecconi, and M. Maksimovic , In-flight calibration of STEREO-B/WAVES antenna system, *Radio Sci.*, *49*, 2014.

Press, W., S. Teukolski, W. Vetterling, and B. Flannery (Eds.), Numerical Recipes in C: The Art of Scientific Computing, 2nd ed., Cambridge Univ. Press, Cambridge, 1992

Rucker, H.O., W. Macher, R. Manning, and H. P. Ladreiter, Cassini model rheometry, *Radio Sci.,* 31, 1299-1311, 1996.

Rucker, H.O., W. Macher, G. Fischer, T. Oswald, J.-L. Bougeret, M. Kaiser, and K. Goetz, Analysis of spacecraft antenna systems: Implications for STEREO/WAVES, *Adv. Space Res.,* 36, 1530–1533, doi: 10.1016/j.asr.2005.07.060, 2005.

Rucker, H.O., M. Sampl, M. Panchenko, T. Oswald, D. Plettemeier, M. Maksimovic, and W. Macher, Implications of antenna system calibration on spacecraft design and radio data analysis, *Planetary Radio Emissions VII*, Austrian Academy of Sciences Press, Vienna, 475-486, 2011.

Sampl, M., W. Macher, C. Gruber, T. Oswald, H.O. Rucker: Rheometry, the effective length vector and the Resonance mission, E & I, 5, 28-32, 2009.

Sampl, M., T. Oswald, H.O. Rucker, G. Fischer, D. Plettemeier, W.S. Kurth, W. Macher: First assessment of the JUNO/Waves antenna properties, European Geosciences Union General Assembly 2011, Wien, Apr 2011.

Vogl, D. F., et al. (2004), In-flight calibration of the Cassini-Radio and Plasma Wave Science (RPWS) antenna system for direction-finding and polarization measurements, *J. Geophys. Res.*, *109*, A09S17, doi:10.1029/2003JA010261.

Wang, L., and T. D. Carr (), Recalibration of the Voyager PRA antenna for polarization sense measurement, *Astron. Astrophys.*, *281*, 945–954, 1994.